



## Au decorated Pd nanowires for methane oxidation to liquid C1 products

Yueshan Xu<sup>1</sup>, Daoxiong Wu<sup>1</sup>, Peilin Deng<sup>\*</sup>, Jing Li, Junming Luo, Qi Chen, Wei Huang, Chong Michael Shim, Chunman Jia, Zhongxin Liu, Yijun Shen, Xinlong Tian<sup>\*</sup>

*State Key Laboratory of Marine Resource Utilization in South China Sea, Hainan Provincial Key Lab of Fine Chemistry, School of Chemical Engineering and Technology, Hainan University, Haikou 570228, China*



### ARTICLE INFO

**Keywords:**

Methane oxidation  
Bimetallic PdAu nanowires  
Selectivity  
Reaction mechanism  
Synergistic effects

### ABSTRACT

The direct methane ( $\text{CH}_4$ ) oxidation to high value-added C1 chemicals is a great promising strategy to explore the  $\text{CH}_4$  resource utilization. However, the low activity and selectivity of catalytic performance remains a great conundrum due to the difficulty to activate the C—H bond and the unmanageable over oxidation. Herein,  $\text{Pd}_x\text{Au}_y$  nanowires (NWs) with various Pd/Au atomic ratios are presented as ideal models to explore the atomic-level effect of PdAu atoms for the direct  $\text{CH}_4$  oxidation. The influence of reaction parameters are systematically investigated, and  $\text{Pd}_9\text{Au}_1$  NWs display a maximum yield of  $2890.3 \mu\text{mol g}^{-1} \text{h}^{-1}$  with 99% selectivity for the liquid C1 oxygenated products. This enhanced performance is attributed to the combination of one-dimensional structure and the synergistic effect from the suitable portion of Au on Pd sites, which regulates bond strength between adsorbed radicals ( $\bullet\text{OH}$ ,  $\bullet\text{OOH}$ ,  $\bullet\text{CH}_3$ ) and PdAu atoms, confirmed by the density function theory calculations.

### 1. Introduction

$\text{CH}_4$  is a highly efficient and clean energy that widely distributed in the earth's crust and oceans.  $\text{CH}_4$  oxidation to high added-value chemical feedstocks such as olefins, aromatics, and small molecule alcohols not only meet various chemical materials, but also realize the efficient  $\text{CH}_4$  resource utilization.<sup>[1–3]</sup> Due to the extremely high bond energy ( $439.3 \text{ kJ}\cdot\text{mol}^{-1}$ ) and weak polarity of the C—H bond in  $\text{CH}_4$  molecule, the activation of C—H bond is very challenging.<sup>[4,5]</sup> In addition, the highly active intermediates from the  $\text{CH}_4$  activation are prone to be over-oxidized or a complete oxidation to carbon dioxide ( $\text{CO}_2$ ), which severely decrease the selectivity of target products.<sup>[6–9]</sup> Currently,  $\text{CH}_4$  is firstly converted into syngas ( $\text{H}_2$  and  $\text{CO}$ ) by the water vapor reforming method, and afterwards  $\text{CH}_3\text{OH}$  is obtained by the Fischer-Tropsch synthesis through the indirect steps.<sup>[10–12]</sup> These processes are quite complicated and require harsh reaction conditions as well as energy-consuming.<sup>[13–16]</sup> Therefore, the direct  $\text{CH}_4$  partial oxidation to C1 chemicals with high activity and selectivity is greatly desirable under relatively mild conditions.

Recently, bimetallic PdAu have emerged as a representative catalyst for the direct  $\text{CH}_4$  oxidation under mild conditions with  $\text{H}_2\text{O}_2$  as the oxidant.<sup>[17–20]</sup> Hutchings et al. reported a radical reaction mechanism

involving methyl ( $\bullet\text{CH}_3$ ) and hydroxyl ( $\bullet\text{OH}$ ) radicals for the oxidation of  $\text{CH}_4$  using PdAu nanoparticles.<sup>[17]</sup> Agarwal et al. used Au-Pd colloids nanoparticles to catalyze  $\text{CH}_4$  to  $\text{CH}_3\text{OH}$  with a selectivity of 92%, and the isotopically labeled reactions confirmed that two thirds of  $\text{H}_2\text{O}_2$  generated  $\bullet\text{OH}$  to excite  $\bullet\text{CH}_3$  generation, and the rest  $\text{H}_2\text{O}_2$  were decomposed to  $\text{O}_2$  into the primary products.<sup>[21]</sup> The introduction of excessive  $\text{O}_2$  could improve the catalytic efficiency by inhibiting the  $\text{H}_2\text{O}_2$  decomposition and promoting  $\text{CH}_3\text{OH}$  formation. Zhu et al. designed PdAu nanoparticles locked in a zeolite molecular sieve (ZSM-5) with a layer of hydrophobic long-chain alkanes ( $\text{C}_{16}$ ) on the surface.<sup>[22]</sup> Due to the "molecular fence" effect, in-situ generated  $\text{H}_2\text{O}_2$  from  $\text{H}_2$  and  $\text{O}_2$  was enclosed in the ZSM-5- $\text{C}_{16}$ , leading to high local concentration of  $\text{H}_2\text{O}_2$ , which significantly improved the utilization of  $\text{H}_2\text{O}_2$  and the conversion rate of  $\text{CH}_4$ . These literatures definitely indicated that PdAu nanoparticles could be used as unique and excellent catalysts for  $\text{CH}_4$  oxidation. However, the exploration of PdAu catalysts mainly focus on the zero-dimensional (0D) structure with unfavorable structure regulation and size control.<sup>[21–23]</sup> In addition, little has been done on verifying the optimal Au/Pd ration or compositions for maximizing the C1 oxygenated yield and selectivity. Furthermore, few works are reported on revealing the structure-activity relationship and the catalytic mechanisms of  $\text{CH}_4$  oxidation is extremely lacking and unclear, not to

\* Corresponding authors.

E-mail addresses: [dengpeilin@hainanu.edu.cn](mailto:dengpeilin@hainanu.edu.cn) (P. Deng), [tianxl@hainanu.edu.cn](mailto:tianxl@hainanu.edu.cn) (X. Tian).

<sup>1</sup> Y. Xu and D. Wu contributed equally to this work.

mention the precise reaction paths for the oxidation to C1 oxygenated chemicals.<sup>[24,25]</sup> Generally, one dimensional (1D) NWs displays improved durability and activity owing to the inherent anisotropic, high specific surface area, high conductivity, fast mass transport and excellent flexibility than those of their zero dimensional (0D) counterparts.<sup>[26,27]</sup> In addition, the 1D structure with extended surface may also provide a desirable model to facilely modulate the geometric and electronic effects by tuning the compositions.

Inspired by above motivations, herein, we report for the first time that Pd<sub>x</sub>Au<sub>y</sub> NWs with different Pd/Au atomic ratios are prepared by a facile galvanic replacement reaction, and applied for the efficient CH<sub>4</sub> oxidation under mild conditions. By regulating the Pd/Au ratios and the reaction parameters, including CH<sub>4</sub> concentration, reaction temperature, reaction time, and catalyst amount, the highest C1 productivity of 2890.3 μmol g<sup>-1</sup> h<sup>-1</sup> with 99% selectivity is realized on Pd<sub>9</sub>Au<sub>1</sub> NWs at 70 °C. Comprehensive structural and catalytic characterizations, as well as the density functional theory calculations, demonstrate that the binding affinity between Pd and •CH<sub>3</sub> is so strong that not only restrain the follow-up reactions to C1 liquid, but also resulting in the over oxidation of CH<sub>4</sub> to CO<sub>2</sub>. This strong binding affinity can be modulated and weakened by the cooperation of Au, and the follow-up processes is accelerated due to the low reaction barrier of CH<sub>3</sub>OH/CH<sub>3</sub>OOH formation. In addition, the over oxidation of CH<sub>4</sub> could be limited, endowing a high selectivity to liquid C1 oxygenated products. In a word, the considerable performance and selectivity of Pd<sub>9</sub>Au<sub>1</sub> NWs can be attributed to the unique structural and synergistic effects induced by the proper Au decorated Pd sites.

## 2. Experimental section

### 2.1. Materials

Sodium tetrachloropalladate (II) (Na<sub>2</sub>PdCl<sub>4</sub>) and Gold chloride trihydrate (HAuCl<sub>4</sub>·3H<sub>2</sub>O), Potassium titanium oxalate, 1,2-dichloropropane (99%) was purchased from MACKLIN reagent. Poly (vinylpyrrolidone) (PVP, ~55000), oleylamine (technique grade, 70%, OM) was purchased from Energy Chemical. Potassium iodide (KI) was purchased from Aladdin. Deionized water was used from Smart-mini System (Nison Instrument (Shanghai) Limited) in all our experiments. All chemicals were used as received without further purification.

### 2.2. Preparation of ultrafine Pd nanowires

Typically, 20 mL PVP aqueous solution (0.04 g/mL) was transferred into a 50 mL Teflon-lined cup under magnetic stirring of 800 rpm. Meanwhile, 6 mL KI aqueous solution (0.1667 g/mL) was added into the Teflon-lined cup with 0.5 mL/min by automatic samplers over 20 min. Subsequently, 10 mL Na<sub>2</sub>PdCl<sub>4</sub> aqueous solution (3.6 mg/mL) was added into the Teflon-lined at 0.5 mL/min. After 40 min, the mixture solution was then transferred into a 50 mL stainless autoclave and heated at 200 °C for 2 h. After cooling to room temperature naturally, the solid products were collected by centrifuging at 12,000 rpm for 0.5 h and further purified by deionized water 4 times to get out of excess ions and PVP molecules. Finally, the obtained Pd nanowires (NWs) were re-dispersed into 8 mL deionized water for further using.

### 2.3. Preparation of Pd<sub>x</sub>Au<sub>y</sub> bimetallic nanowire

8 mL of 1.25 mg/mL Pd nanowires seeds, 105 mg of PVP, and a certain amount (Table S1) of HAuCl<sub>4</sub> (100 mg/mL) were mixed in a 20 mL glass bottle and held at 60 °C for 3 h under magnetic stirring. After cooling down to room temperature, the solid products were collected by centrifuging at 12,000 rpm for 0.5 h and further purified by a deionized water 5 times to get out of free PVP molecules and ionic species. Finally, the samples were re-dispersed into 10 mL deionized water for further using.

### 2.4. Preparation of ultrafine Au nanowires

Typically, 4.8 mL of OM and 1.2 mL of 1,2-dichloropropane were vortexed well in 10 mL centrifuge tubes and placed in an ice bath for 2 min, followed by rapid addition to a glass vial containing 3 mg of HAuCl<sub>4</sub>·3 H<sub>2</sub>O with continued vortex shaking well. The glass vials were sealed and heated in an oil bath at 70 °C for 17 h. The resulting product was collected by centrifugation (3000 rpm, 3 min), washed three times with hexane and then re-dispersed in hexane.

### 2.5. Characterization of Pd NWs and Pd<sub>x</sub>Au<sub>y</sub> bimetallic nanowire

Transmission Electron Microscope (TEM) images, High-angle annular dark-field scanning transmission electron microscopy (HAADF-STEM) images of samples were recorded on a thermoscientific Talos F200X G2 high-resolution transmission electron microscope at 200 kV. X-ray diffraction (XRD) patterns of samples were conducted on a Rigaku Smart-Lab operating at the voltage of 40 kV and the current 40 mA with Cu Ka radiation ( $\lambda = 1.5406 \text{ \AA}$ ). X-ray photoelectron spectroscopy (XPS) was conducted on Shimadzu Axis Supra using a Al Ka ( $h\nu = 1486.6 \text{ eV}$ ) radiation source. The Pd/Au atomic ratio was determined by inductively coupled plasma-atom emission spectroscopy (ICP-AES, Agilent 7700). Proton nuclear magnetic resonance (<sup>1</sup>H NMR) (CH<sub>3</sub>OH, CH<sub>3</sub>OOH and HCOOH) were tested by adding 300 μL electrolyte into the 250 μL D<sub>2</sub>O (deuterated water) and 25 μL dimethyl sulfoxide solution (6 mM), in which DMSO was used as an internal standard. The one-dimensional <sup>1</sup>H NMR spectrum was measured with water suppression at 4.7 ppm by using a pre-saturation method. The <sup>1</sup>H spectrum peaks of CH<sub>3</sub>OH, CH<sub>3</sub>OOH and HCOOH are at ~3.3, ~3.6 and ~8.3 ppm, respectively. The <sup>1</sup>H spectrum peak of DMSO is at ~2.6 ppm. Afterward, CH<sub>3</sub>OOH was converted to CH<sub>3</sub>OH by using hydrazine hydrate (100 μL). The total amount of CH<sub>3</sub>OH and CH<sub>3</sub>OOH were analyzed by gas chromatograph (GC), and the amount of CH<sub>3</sub>OOH was obtained by minusing method. The gas products were tested by GC (Trace 1300 Series, Thermo Fisher) with flame ionization detector (FID). The CO and CO<sub>2</sub> could be converted into CH<sub>4</sub> through the methanator and analyzed by FID. The content of all products was calculated by using the standard curve method. The productivity and the selectivity of all products were calculated by using the following formula (1) and (2).

$$\text{The productivity of products} (\mu\text{mol g}^{-1} \text{ h}^{-1}) = \frac{\text{Products}(\mu\text{mol})}{\text{Catalyst(g)} \times \text{Time(h)}} \quad (1)$$

$$\text{Liquid product selectivity}(\%) = \frac{\text{CH}_3\text{OH} + \text{CH}_3\text{OOH} + \text{HCOOH}(\mu\text{mol})}{\text{All products}(\mu\text{mol})} \times 100\% \quad (2)$$

### 2.6. Catalytic performance of the direct conversion of CH<sub>4</sub>

Methane oxidation was carried out in a 50 mL stainless-steel autoclave containing a quartz liner vessel with 10 mL of colloidal catalyst. The autoclave was sealed and purged three times with feed gas containing 3.3% H<sub>2</sub>, 6.6% O<sub>2</sub>, 1.6% CH<sub>4</sub>, and 61.7% Ar, and 26.8% He and maintaining the pressure at 1.0 MPa. The mixture was stirred at 1200 rpm and heated to specific temperature at the ramp rate of 1.5 °C/min, followed by introducing the feed gas CH<sub>4</sub> and maintaining the pressure at 3.0 MPa, maintained at the reaction temperature for 0.5 h. At the end of reaction, the autoclave was cooled in ice to a temperature below low than 10 °C in order to minimize the loss of volatile products. In order to study the reusability of the catalyst, the colloidal catalyst was separated by centrifugation (12,000 rpm/30 min) after each reaction run. After drying at 80 °C for 12 h in vacuum, the catalyst was reused in the next run.

## 2.7. The turnover frequency (TOF) of the as-prepared catalysts

$$TOF = \frac{\text{Turnover number for oxygenate formation (TON)}}{\text{Number of active site (N)}}; \text{ units is h}^{-1}$$

$$TON = n(\text{oxygenate}) \times N_A;$$

$n$  is the amount of substance of the oxygenated products;  $N_A$  is  $6.02 \times 10^{23}$ .

$$N = \frac{m \times W}{M} \times N_A$$

$N$  is Number of active sites,  $m$  is the amount of substance of Pd,  $M$  is the relative atomic mass of Pd,  $W$  is the mass fraction of Pd in the catalyst.

## 2.8. Electron paramagnetic resonance (EPR) test

The detection of free radicals in the reaction process of direct methanol oxidation was performed at a Bruker A320 electron paramagnetic resonance spectroscopy (EPR, Field setting resolution: 1MG (0.1UT)), using 5, 5'-dimethyl-1-pyrroline-N-oxide (DMPO) was used as the scavenger. Typically, 1 mL DMPO-H<sub>2</sub>O (100 mmol L<sup>-1</sup>) was added into 1 mL of reaction mixture. Transfer the mixed solution immediately to the capillary tube (diameter: 0.1 mm; filling liquid height: ~ 5 cm), which was then fixed in the resonant cavity of the spectrometer. Contrast experiments were carried out to determine the type of free radical by the characteristic peaks. Contrast experiment 1 (No. 1) (labeled as DMPO + H<sub>2</sub>O<sub>2</sub> + Fe<sup>2+</sup>): 1 mL FeSO<sub>4</sub>·7 H<sub>2</sub>O (50 mmol L<sup>-1</sup>) and HNO<sub>3</sub> solution (pH = 4) were mixed with 1 mL DMPO-H<sub>2</sub>O (100 mmol·L<sup>-1</sup>) under vortex oscillation g for 2 min, followed by adding 50 μL of H<sub>2</sub>O<sub>2</sub> (30 wt%). No. 2 (labeled as DMPO + H<sub>2</sub>O<sub>2</sub> + Fe<sup>2+</sup> + CH<sub>3</sub>OH): all the processes were the same with contrast experiment 1, except for the addition of 1 mL of CH<sub>3</sub>OH (100 mmol L<sup>-1</sup>) into the solution.

## 2.9. CH<sub>4</sub> temperature-programmed desorption (CH<sub>4</sub>-TPD) test

Firstly, 50 mg of the sample was weighed into a reaction tube and dried at 10 °C/min from room temperature to 400 °C. The sample was purged with argon gas (50 mL/min) for 1 h and cooled to 50 °C. In turn, a 5% v/v CH<sub>4</sub>/Ar mixture (50 mL/min) is passed through the catalyst base at 50 °C for 0.5 h. And, the Ar gas stream (50 mL /min) was switched for 0.5 h at the same temperature to remove weakly physically adsorbed CH<sub>4</sub> from the surface. Finally, the gas was desorbed under Ar atmosphere at a rate of 5 °C/min to 400 °C and detected by TCD.

## 2.10. Density functional theory (DFT) calculation

Spin-polarized density functional theory calculations were performed by using the Vienna *Ab Initio* Simulation Package (VASP) [28, 29]. The PBE [30] functional and the projector augmented wave (PAW) [31,32] potential were employed. An energy cutoff of 500 eV and a convergence criterion of 10<sup>-5</sup> eV for self-consistent calculations was adopted. The Pd slab exposed (111) surface with 4 × 4 × 1 supercell and four metal layers were cleaved from the bulk materials and the thickness of the vacuum layer between adjacent slab models was about 15 Å. All structures were fully relaxed until the total force on each atom was less than 0.05 eV/ Å. The first Brillouin zone was sampled using a 4 × 4 × 1 Γ-centered k-point mesh. The van der Waals interactions were corrected based on the DFT-D3 scheme [33,34]. COHP [35–37] analysis as implemented in the LOBSTER code<sup>38</sup> was carried out with the pbe-VaspFit2015 basis set [38]. The corresponding basis functions of H, C, O, Pd, and Au were 1 s, 2s2p, 2s2p, 4d5s, and 5d6s, respectively. The energy barriers were calculated by using the climbing image nudged elastic

band (CI-NEB) method [39]. The solvent effect was included by using the implicit solvation model as implemented in the VASPsol code [40, 41].

The adsorption energy of the molecule on the surface was defined as  $E_{\text{ad}} = E_{\text{system}} - E_{\text{slab}} - E_{\text{molecule}}$ , where the  $E_{\text{system}}$ ,  $E_{\text{slab}}$ , and  $E_{\text{molecule}}$  are the DFT energy of the slab system with molecule adsorbed on the surface, the slab system, and one adsorbed molecule. VASPkit code [42] and VESTA software [43] were used for calculation pre-processing and post-processing.

## 3. Results and discussion

### 3.1. The preparation and characterizations for Pd<sub>x</sub>Au<sub>y</sub> NWs

Fig. 1a illustrates the synthesis process of Pd<sub>x</sub>Au<sub>y</sub> NWs by the self-assemble and galvanic replacement method, and the effects of KI and PVP concentrations, reaction temperature and reaction time on the morphology of Pd NWs are systematically investigated (Fig. S1). The average diameter of highly purified Pd NWs is approximately 7.2 nm with some concave and convex sites on the surface of Pd NWs, and the crystal plane spacing of 0.225 and 0.195 nm corresponds well to the (111) and (200) crystal planes of Pd, respectively (Fig. S2). Then a series of high quality Pd<sub>x</sub>Au<sub>y</sub> NWs with different Pd/Au atomic ratios were rapidly synthesized by tuning the content of Au salt precursors (Figs. S3, S4) [44].

Representative transmission electron microscope (TEM) images show that Pd<sub>9</sub>Au<sub>1</sub> NWs exhibits a uniform and serrated morphology with a few microns in length (Fig. 1b). The average diameter of the Pd<sub>9</sub>Au<sub>1</sub> NWs at the widest and narrowest positions are 12.9 nm and 6.5 nm, respectively (Fig. S3). The element mapping result shows that Pd elements are mainly distributed in the middle, while Au elements are on the surface of the Pd<sub>9</sub>Au<sub>1</sub> NWs, especially the protruding parts of the serrated structure (Fig. 1c). Corresponding EDS elemental analysis result shows that the Pd/Au atomic ratio is close to the value of 9:1 (Fig. 1d). To further track the microstructure of the Pd<sub>9</sub>Au<sub>1</sub> NWs, the concave and convex areas are characterized in detail (Fig. 1e-g). As shown in the high-resolution TEM (HRTEM) image of concave part, the interplanar spacing of 2.247 Å is indexed as (111) crystal planes of the inner Pd NWs, while the interplanar spacing of 2.433 Å is attributed to the (111) crystal plane of the outer Au atoms (Fig. 1g). The selected Fourier transform (FTT) results for the inner and outer areas (light blue boxes) show that the crystal orientation of Pd<sub>9</sub>Au<sub>1</sub> NWs is consistent with the results of the HRTEM, and there also is a five-fold twinned structure (Fig. 1h, 1i). The atomic diameter of Pd and Au atoms is 0.273 nm and 0.286 nm, respectively, consistent with the theoretical diameters (Fig. 1j). In addition, with increasing of Au content, the structure of Pd<sub>x</sub>Au<sub>y</sub> NWs gradually changes from a smooth surface to a bead-like structure (Fig. S4). HRTEM images show that Pd NWs are covered by a few Au atoms, and the crystal spacing of Pd atoms gradually decreases due to the compressive strain introduced by the outer Au atoms. Moreover, the corresponding EDS results further demonstrate the precise control for the compositions of Pd<sub>x</sub>Au<sub>y</sub> NWs by using the galvanic replacement method (Fig. S5). To further confirm the actual chemical compositions of Pd<sub>x</sub>Au<sub>y</sub> NWs, Pd/Au atomic ratios are obtained from ICP-AES results, which is in agreement with EDS results (Table S2).

X-ray diffraction (XRD) is performed to explored the crystalline structure of Pd<sub>x</sub>Au<sub>y</sub> NWs (Fig. 2a). Pd NWs is a face-centered cubic structure with the space group  $Fm\bar{3}m$ , and the crystal plane of (111) and (200) correspond to the lattice spacing of 0.225 nm and 0.195 nm, respectively, in accordance with the HRTEM results [45]. The crystalline structure of Pd<sub>x</sub>Au<sub>y</sub> NWs is still similar with the Pd NWs with increasing the Au content because of the low content of Au element. However, the peaks of (111) and (200) crystal planes are shifted towards a higher angle, suggesting the lattice spacing of Pd atoms becomes smaller due to the compression effect resulted from the outer Au atoms, in agreement

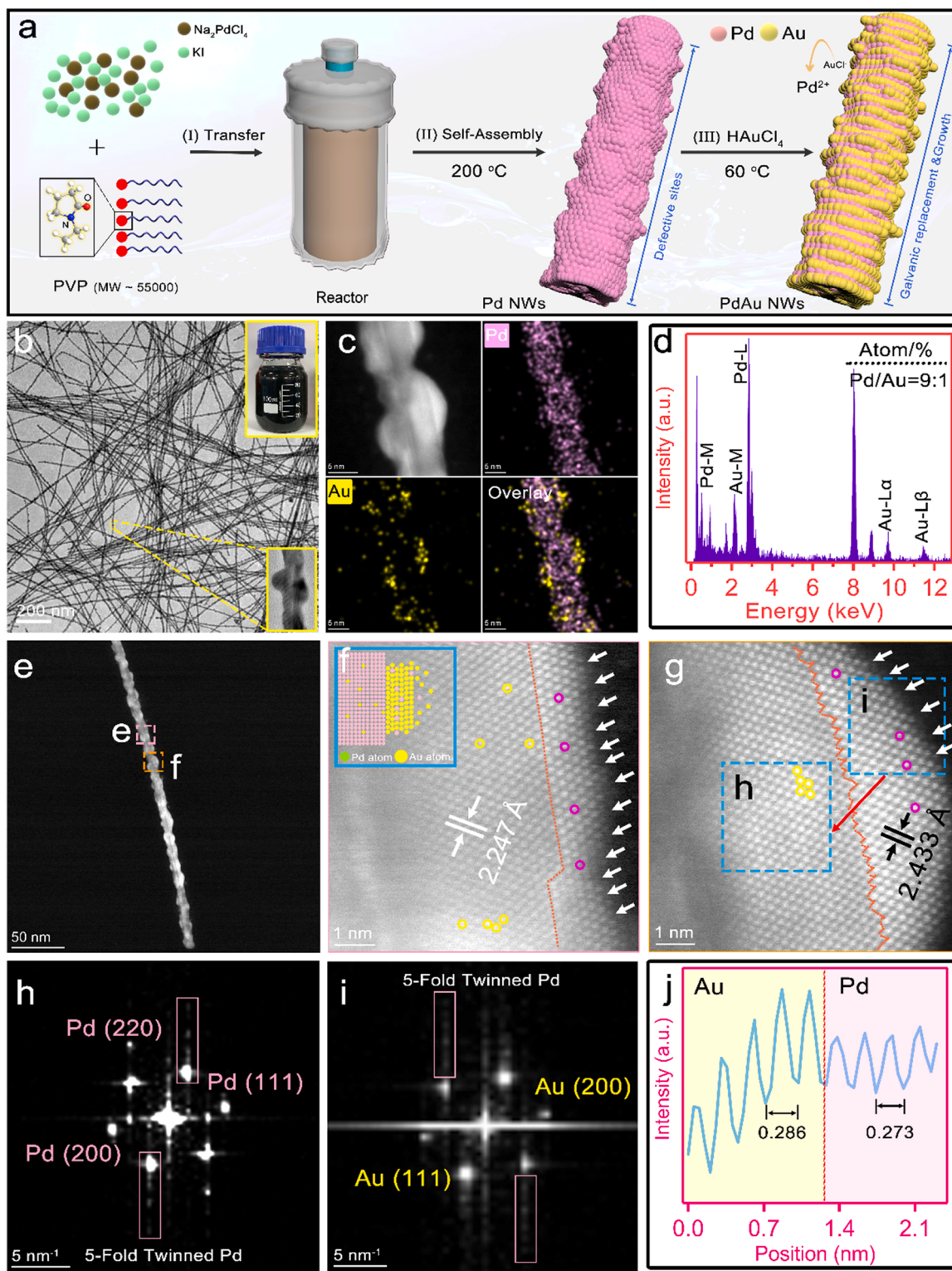


**Fig. 1.** (a) Schematic illustrations for the synthesis of  $\text{Pd}_x\text{Au}_y$  NWs. (b) TEM image of  $\text{Pd}_9\text{Au}_1$  NWs (Upper inset: photograph of the as-prepared colloid solution of  $\text{Pd}_9\text{Au}_1$  NWs; bottom inset: magnified image of the region in the yellow box). (c) High-angle annular dark-field scanning transmission electron microscopy (HADDF-STEM) images and the corresponding STEM-EDS element mapping of  $\text{Pd}_9\text{Au}_1$  NWs. (d) TEM-EDS spectrum of  $\text{Pd}_9\text{Au}_1$  NWs. (e) HADDF-STEM image of a single  $\text{Pd}_9\text{Au}_1$  NW. (f, g) HRTEM images corresponding to the (e). (h-i) FFT pattern corresponding to (g). (j) Intensity profiles of element along the red lines in (f). (For interpretation of the references to colour in this figure, the reader is referred to the web version of this article.)

with the TEM results (Fig. 2b). X-ray photoelectron spectroscopy (XPS) can reflect the surface chemical state and electronic structure of  $\text{Pd}_x\text{Au}_y$  NWs. As shown in Fig. 2c, the peaks at 335.0 and 340.3 eV are attributed to the  $3d_{5/2}$  and  $3d_{3/2}$  of metal  $\text{Pd}^0$  respectively. Compared with

peaks of Pd NWs, the  $3d$  peaks of  $\text{Pd}_x\text{Au}_y$  NWs exhibit a slight decrease, except for  $\text{Pd}_7\text{Au}_1$  with higher Au content, which resulted from the litter Au atoms inducing the interaction between Pd and Au atoms. In addition, the oxidized  $\text{Pd}^{2+}$  species are also detected, corresponding to peaks

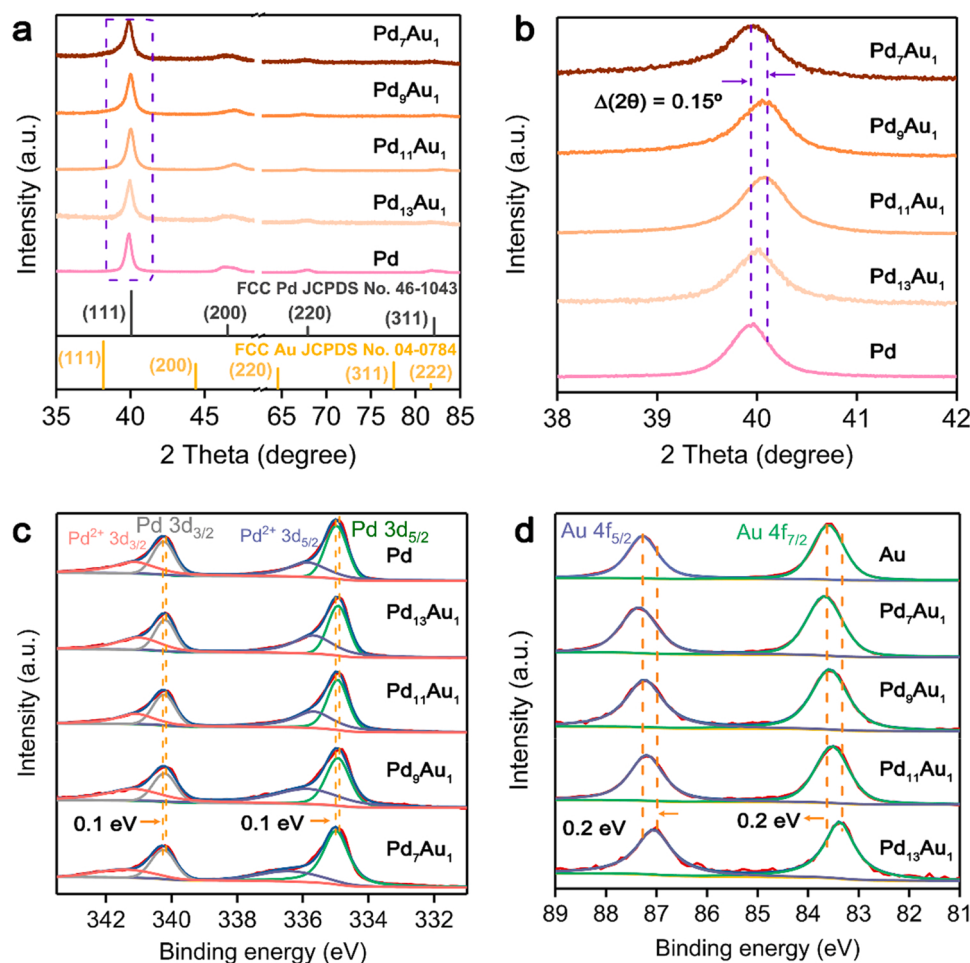


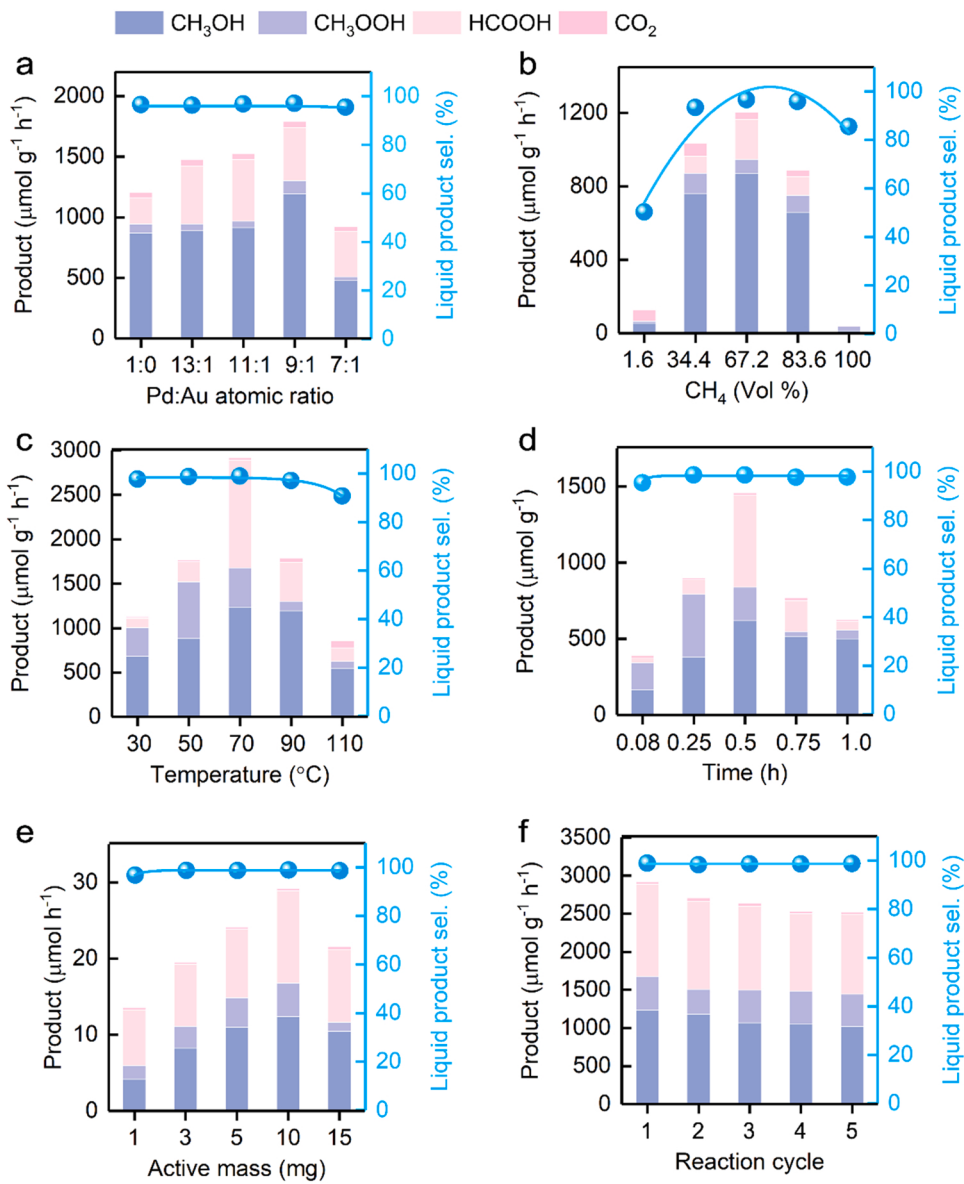
**Fig. 2.** (a) XRD patterns of Pd and  $\text{Pd}_x\text{Au}_y$  NWs. (b) The magnified image of the region around the crystal face of (111). (c) XPS spectrums of Pd 3d for Pd NWs and  $\text{Pd}_x\text{Au}_y$  NWs. (d) XPS spectrums of Au 4f for Au and  $\text{Pd}_x\text{Au}_y$  NWs.

of 335.9 eV ( $3d_{5/2}$ ) and 341.2 eV ( $3d_{3/2}$ ), respectively, which may be ascribed to the property of easily oxidized Pd atoms in air. As shown in Fig. 2d, the peaks at 83.7 and 87.2 eV are attributed to the  $4f_{7/2}$  and  $4f_{5/2}$  of the metal  $\text{Au}^0$ , respectively. The electronic states of 4f peaks shift towards a lower binding energy, indicating the electrons enrichment of Au atoms. The simultaneous negative shift of Pd 3d and Au 4f are attributed that the electrons transfer from inner orbit to outer orbit, demonstrating that the external Au atoms affect the electronic structure of Pd atoms [45]. Moreover, the surface Pd/Au atom ratio in XPS results is obviously higher than the whole Pd/Au atom ratio in the TEM-EDS results because of the Au atom covering the surface of Pd NWs (Table S3).

### 3.2. The catalytic performance for the direct $\text{CH}_4$ conversion

The catalytic performance of the direct  $\text{CH}_4$  oxidations is measured in a sealed pressurized stainless-steel reactor. The gas and liquid products are quantified by gas chromatography (GC) and proton nuclear magnetic resonance ( $^1\text{H}$  NMR), and the corresponding plots and standard curves of which are shown in Figs. S6-S8. As shown in Fig. 3a, Pd NWs catalyst exhibits a productivity of  $1163.1 \mu\text{mol g}^{-1} \text{h}^{-1}$  and a selectivity of 96.6% for  $\text{CH}_4$  converting to liquid C1 oxygenated products, higher than that of Pd nanoparticles [21,25], which is attributed to the special property of one-dimensional structure. With the decoration of Au atoms,  $\text{Pd}_x\text{Au}_y$  NWs present a higher productivity and selectivity for C1 products (Fig. S9 and Table S4). Obviously,  $\text{Pd}_9\text{Au}_1$  NWs shows a highest catalytic performance via precisely adjusting the Pd/Au atomic

ratios, corresponding to the productivity of  $1738.5 \mu\text{mol g}^{-1} \text{h}^{-1}$  and the selectivity of 97.1% at  $90^\circ\text{C}$ , which indicate that  $\text{Pd}_9\text{Au}_1$  catalysts well activate  $\text{CH}_4$  molecule and suppress the over oxidation of  $\text{CH}_4$  for direct  $\text{CH}_4$  oxidations to liquid C1 products. The comparison results demonstrate that Pd is the active site during direct  $\text{CH}_4$  oxidation, and there is not activity for Au atom (Table S5). With the decoration of Au atoms into Pd NWs,  $\text{Pd}_x\text{Au}_y$  NWs show a higher catalytic performance for oxygenated products than that of Pd NWs, indicating the incorporation of Au atoms could affect the intrinsic activity of Pd atoms for direct  $\text{CH}_4$  oxidation. To further evaluate intrinsic activity of the Pd NWs and  $\text{Pd}_x\text{Au}_y$  NWs, turnover frequencies (TOFs) are calculated and Pd atoms are served as active sites.  $\text{Pd}_9\text{Au}_1$  NWs has a highest TOF than Pd NWs and other  $\text{Pd}_x\text{Au}_y$  NWs due to the moderate incorporation of Au atoms into Pd NWs. But more incorporation of Au atoms in turn inhibit intrinsic activity of Pd atoms (Table S6). The effect of various reaction conditions ( $\text{CH}_4$  contents, oxidant form, reaction temperature, time and the amount of catalysts) are systematically discussed for the direct conversion of  $\text{CH}_4$ . Firstly, when the  $\text{CH}_4$  content is extremely low, the liquid products are almost not detected (Fig. 3b). However, the appropriate  $\text{CH}_4$  content could obtain a highest yield of liquid C1 products, which prove that the liquid C1 products come from the  $\text{CH}_4$  conversion (Table S7). Secondly, it is consequently essential to investigate suitable reaction temperature and time to improve the performance of the direct  $\text{CH}_4$  conversion. As shown in Fig. 3c, the yield of liquid C1 products behaves an increasing manner from  $30^\circ\text{C}$  to  $70^\circ\text{C}$  with an excellent selectivity. However, the yield and selectivity of liquid products rapidly decrease over  $70^\circ\text{C}$ , and the peroxidation product obviously increased.



These results suggest the improved temperature is beneficial for the higher catalytic activity and selectivity for oxygenated products, but the higher temperature could accelerate the generation of by-products, leading to a lower catalytic activity and selectivity for targeted products. The maximum yield of liquid products is  $2890.3 \mu\text{mol g}^{-1} \text{h}^{-1}$  with a selectivity of 99% at  $70^\circ\text{C}$  for  $\text{Pd}_9\text{Au}_1$  NWs during direct  $\text{CH}_4$  oxidation (Table S8), which is comparable and even much higher than the previously reported literatures (Table S8). When  $\text{H}_2\text{O}_2$  and  $\text{H}_2\text{O}_2/\text{O}_2$  respectively used as the oxidant, the productivity of liquid C1 products for  $\text{Pd}_9\text{Au}_1$  NWs only reaches  $324.7 \mu\text{mol g}^{-1} \text{h}^{-1}$  and  $129.0 \mu\text{mol g}^{-1} \text{h}^{-1}$  (Table S10). These results are dramatic lower than the value ( $2890.3 \mu\text{mol g}^{-1} \text{h}^{-1}$ ) with in situ formation of  $\text{H}_2\text{O}_2$  from  $\text{O}_2$  and  $\text{H}_2$ , which demonstrate that the in-situ  $\text{H}_2\text{O}_2$  generation favors to accelerate  $\text{CH}_4$  oxidation [17,22]. In addition, the yield of liquid C1 products gradually increases with the extension of reaction time, and the reaction time of 0.5 h reaches the highest yield of liquid products (Fig. 3d), while prolonged reaction time leads to the deep oxidation of liquid products to  $\text{CO}_2$  (Table S11). Furthermore, the yield of liquid C1 products increases with increasing the amount of  $\text{Pd}_9\text{Au}_1$  NWs (Fig. 3e), while the yield fleetly decreases with excessive catalysts, which may be explained by the restricted mass transfer (Table S12). Moreover,  $\text{Pd}_9\text{Au}_1$  NWs exhibits

**Fig. 3.** (a) The yield of products and selectivity of liquid products for  $\text{Pd}$  and  $\text{Pd}_x\text{Au}_y$  NWs. Reaction conditions: 0.5 h,  $90^\circ\text{C}$ , 10 mg of catalyst; (b) The catalytic performance with different  $\text{CH}_4$  vol.  $\text{Pd}$  NWs. Reaction conditions: 0.5 h,  $90^\circ\text{C}$ , 10 mg of  $\text{Pd}$  NWs; (c) The catalytic performance with different reaction temperatures for  $\text{Pd}_9\text{Au}_1$  NWs. Reaction conditions: 0.5 h,  $\text{CH}_4$  of 67.2 vol%, 10 mg of  $\text{Pd}_9\text{Au}_1$  NWs. (d) The catalytic performance with different reaction time for  $\text{Pd}_9\text{Au}_1$  NWs. Reaction conditions:  $70^\circ\text{C}$ , 10 mg of  $\text{Pd}_9\text{Au}_1$  NWs. (e) The catalytic performance with different active mass for  $\text{Pd}_9\text{Au}_1$  NWs. Reaction conditions: 0.5 h,  $70^\circ\text{C}$ ,  $\text{CH}_4$  of 67.2 vol%. (f) Reaction tests for the recycle and regeneration of the  $\text{Pd}_9\text{Au}_1$  NWs catalyst. All other conditions remain the same: 10 mL of water, feed gas at 3.0 MPa with 1.1%  $\text{H}_2$ /2.2%  $\text{O}_2$ /67.2%  $\text{CH}_4$ /20.57% Ar/8.93% He, and 1200 revolutions per minute (rpm).

excellent catalytic performance during five cycles, maintaining more than 90% of the initial yield of liquid C1 product as well as negligible variation in selectivity (Fig. 3f). More importantly, there is essentially no change in the morphology can be observed, demonstrating the high cycling and structural stability of  $\text{Pd}_9\text{Au}_1$  NWs (Fig. S11).

### 3.3. Mechanism insights into $\text{CH}_4$ activation and C1 products generation

To clarity the reaction mechanisms of  $\text{Pd}_x\text{Au}_y$  NWs for the direct conversion of  $\text{CH}_4$ , the key reaction steps are analyzed, especially  $\text{CH}_4$  decomposition step and  $\text{H}_2\text{O}_2$  formation step. As illustrated in Fig. 4a, the typical  $^1\text{H}$  NMR spectrum peaks of  $\text{CH}_3\text{OH}$ ,  $\text{CH}_3\text{OOH}$  and  $\text{HCOOH}$  are at  $\sim 3.3$ ,  $\sim 3.6$  and  $\sim 8.3$  ppm, respectively. First of all, the  $\text{CH}_3\text{OOH}$  is mainly formed during the direct  $\text{CH}_4$  oxidation at 0.08 h. With time up to 0.5 h,  $\text{CH}_3\text{OOH}$  showed a decreasing trend, while  $\text{CH}_3\text{OH}$  and  $\text{HCOOH}$  showed an increasing tendency, which heralded a conversion of  $\text{CH}_3\text{OOH}$  to  $\text{CH}_3\text{OH}$  and  $\text{HCOOH}$ . Meanwhile, the in-situ generation of  $\text{H}_2\text{O}_2$  from  $\text{O}_2$  and  $\text{H}_2$  can be occurred with the catalysis of  $\text{PdAu}$  NWs, which is confirmed by the titanium oxalate spectrophotometric method (Fig. S12 and Table S13) [21,22,46]. The generation of  $\text{H}_2\text{O}_2$  is along with the direct  $\text{CH}_4$  oxidation, which demonstrate that the trigger of  $\text{CH}_4$

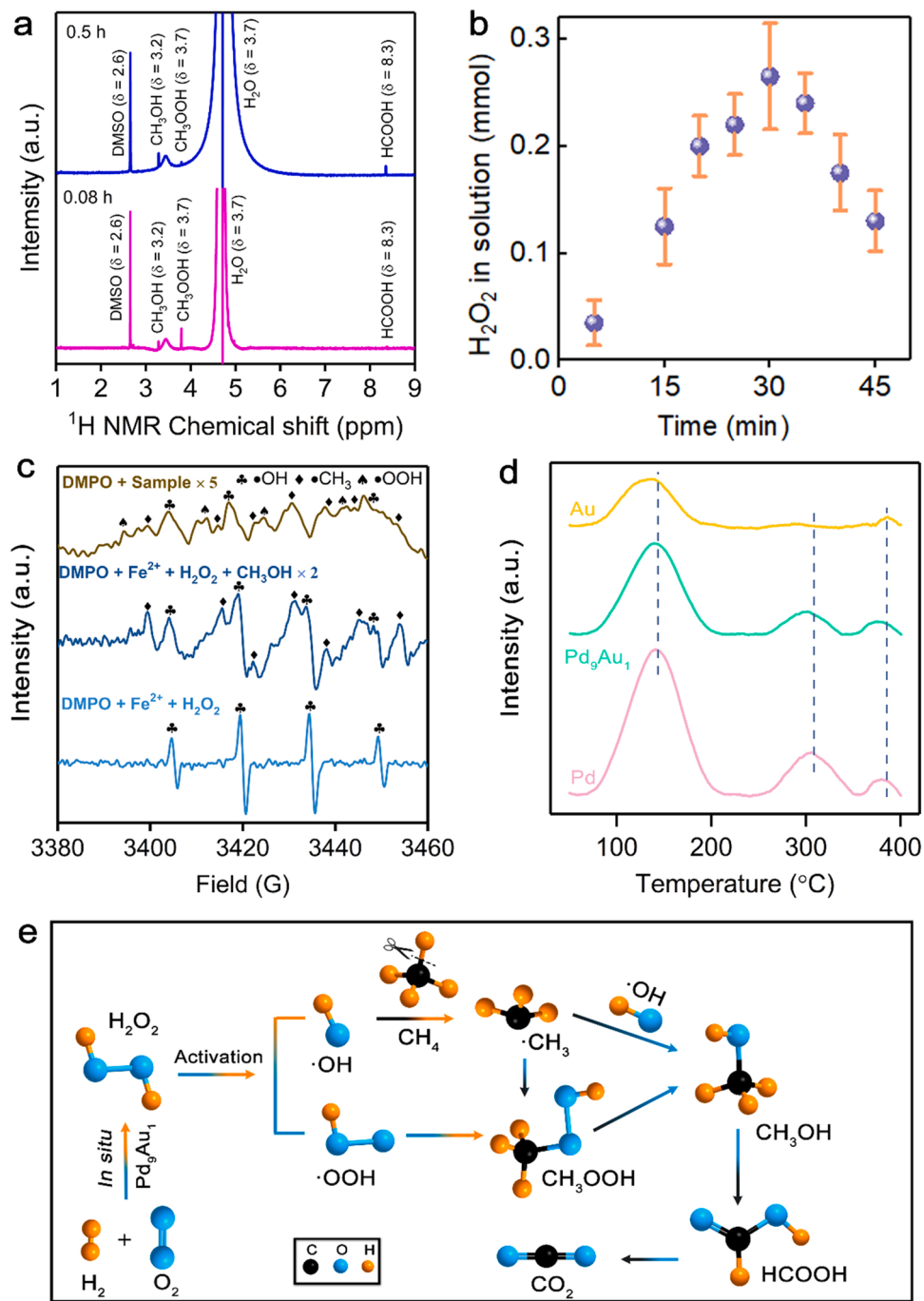


**Fig. 4.** (a) <sup>1</sup>H NMR spectra of liquid products with the reaction time of 0.08 h and 0.5 h, respectively; (b) The time-dependency of in situ generation H<sub>2</sub>O<sub>2</sub> productivity for 90 °C in O<sub>2</sub> and H<sub>2</sub> atmosphere. (c) The signal of EPR spectrum of radical species ( $\bullet\text{CH}_3$ ,  $\bullet\text{OH}$ ,  $\bullet\text{OOH}$ ); (d) CH<sub>4</sub>-TPD of Pd NWs, Au NWs and Pd<sub>9</sub>Au<sub>1</sub> NWs, respectively; (e) The proposed reaction mechanism of the direct CH<sub>4</sub> oxidation to liquid products.

decomposition step requires the presence of  $\bullet\text{OH}$  radical from H<sub>2</sub>O<sub>2</sub> (Fig. 4b). Meanwhile, the content of H<sub>2</sub>O<sub>2</sub> is gradually increasing with reaction time prolonging. The highest content of H<sub>2</sub>O<sub>2</sub> corresponds to the optimal reaction time during the direct CH<sub>4</sub> oxidation. As shown in Fig. 4c (from top to bottom), DMPO (5, 5'-dimethyl-1-pyrroline-N-oxide) is used as the scavenger and additionally (H<sub>2</sub>O<sub>2</sub> + Fe<sup>2+</sup>) and (H<sub>2</sub>O<sub>2</sub> + Fe<sup>2+</sup> + CH<sub>3</sub>OH) are added as contrast experiments, respectively, which show the presence of  $\bullet\text{OH}$ ,  $\bullet\text{OOH}$  and  $\bullet\text{CH}_3$  radicals in the reaction systems, further confirming that the direct CH<sub>4</sub> oxidation is triggered by the free radical process of  $\bullet\text{OH}$ . [17] In addition, the temperature programmed desorption (TPD) not only reflects the binding capacity between the adsorbent and the catalysts surface, but also the

kinetic behavior at the temperature and surface coverage during desorption occurs. As depicted in Fig. 4d, the Au NWs, having a similar structure with Pd NWs (Fig. S13), shows a desorption peak at 130 °C, while Pd NWs has three desorption peaks at 140 °C, 310 °C and 390 °C, respectively. These results indicate that there is a weak CH<sub>4</sub> adsorption capacity for Au NWs to go against the CH<sub>4</sub> activation, which prove the sluggishness of Au NWs for CH<sub>4</sub> direct oxidation as prove by the experiment (Table S4). However, Pd atoms exhibit a strong CH<sub>4</sub> adsorption capacity, while the strong interaction may lead to the difficulty in the subsequent processes for the CH<sub>4</sub> oxidation. With the addition of Au, the desorption peaks move towards the lower temperature and a much higher performance for CH<sub>4</sub> oxidation is obtained,

which proves that the moderate adsorption capacity is beneficial for the  $\text{CH}_4$  activation and the following generation of liquid C1 products. Therefore, based on above results, the reaction mechanisms for the conversion of  $\text{CH}_4$  to liquid C1 products are proposed with three steps (Fig. 4e): (1) Firstly, the  $\text{H}_2\text{O}_2$  is in situ generation from  $\text{O}_2$  and  $\text{H}_2$  by catalyzed PdAu NWs, then which could form  $\bullet\text{OH}$  and  $\bullet\text{OOH}$  radicals; (2) Simultaneously,  $\text{CH}_4$  adsorbed on PdAu NWs surface is activated with  $\bullet\text{OH}$  to form  $\bullet\text{CH}_3$  radical by controllable breaking the C-H bond; (3) The combination of  $\bullet\text{CH}_3$  radical with  $\bullet\text{OH}$  or  $\bullet\text{OOH}$  radicals to form  $\text{CH}_3\text{OH}$  or  $\text{CH}_3\text{OOH}$ , respectively. Then  $\text{CH}_3\text{OOH}$  fast converts to  $\text{CH}_3\text{OH}$ , which could be over-oxidized to a spot of  $\text{HCOOH}$  and  $\text{CO}_2$  products via a multi-step radical activation process.

#### 3.4. Effect of Au atoms decorated Pd NWs for $\text{CH}_4$ conversion

The density function theory (DFT) calculations are carried out to further illuminate theoretical insights into the mechanisms of  $\text{CH}_4$  oxidation on PdAu NWs. Two slab models, Pd slab and PdAu slab, are displayed in Fig. 5a and Fig. 5b, respectively. As summarized in Table S14, the adsorption of  $\text{CH}_3^*$ ,  $\text{OH}^*$ , and  $\text{OOH}^*$  on Pd surface is

strong with a large adsorption energy ( $E_{\text{ad}}$ ) of  $-2.11$ ,  $-2.70$ , and  $-1.31$  eV, respectively, while it's relatively weak with a smaller  $E_{\text{ad}}$  of  $-1.88$ ,  $-2.21$ , and  $-0.92$  eV on the PdAu surface. The corresponding adsorption configurations of Pd and PdAu slab are displayed in Fig. 5c and Fig. 5d, respectively. The integrated crystal orbital Hamilton population (ICOHP) at the Fermi level between the adsorbent and the slab, which has got great success to correlate the adsorption strength with the electronic structure [47–50], is calculated. A more negative ICOHP indicates the stronger chemical bond between the adsorbed radicals and the surface. As shown in Fig. 5e and Table S15, the ICOHP for  $\text{CH}_3^*$ ,  $\text{OH}^*$ , and  $\text{OOH}^*$  on Pd surface is  $-2.44$ ,  $-3.31$ , and  $-3.34$ , respectively, while it's  $-2.31$ ,  $-2.04$ , and  $-2.08$  on PdAu surface. These results demonstrate that the existence of Au enables to modulate the interactions between the intermediates and Pd atoms (Fig. S14 and Table S15), leading to a weaker adsorption strength for the intermediates on the PdAu surface, which offers opportunity to optimize the  $\text{CH}_4$  conversion performance.

Both of the  $\text{CH}_3\text{OH}$  and  $\text{CH}_3\text{OOH}$  paths are investigated on the Pd and PdAu surface, and each path can be divided into two stages (Figs. 5f and 5g), that is, the  $\text{CH}_4$  activation stage (stage-I) and  $\text{CH}_3\text{OH}$  (or

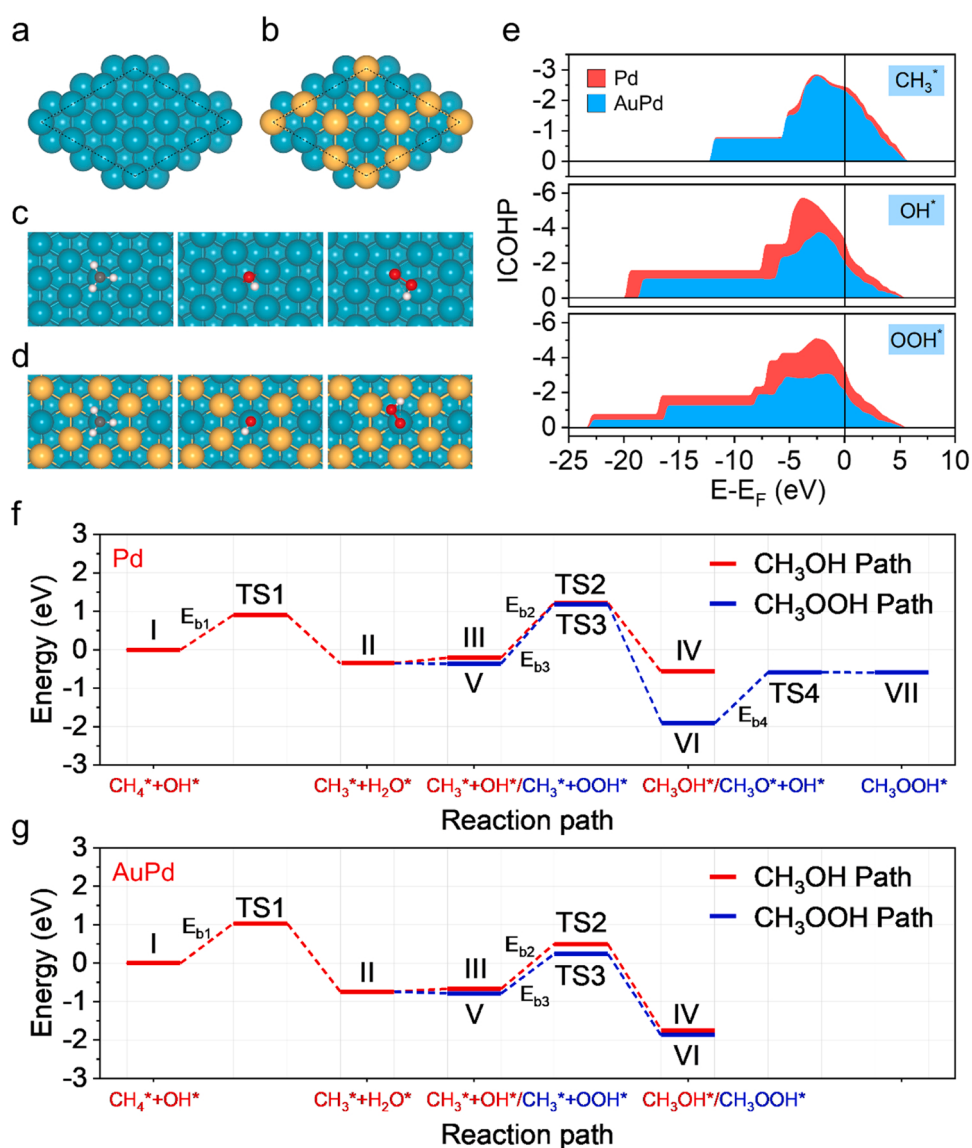


**Fig. 5.** Crystal structure of (a) Pd slab and (b) PdAu slab. Adsorption configuration of  $\text{CH}_3^*$ ,  $\text{OH}^*$ , and  $\text{OOH}^*$  on (c) Pd slab and (d) PdAu slab. (e) ICOHP results. Reaction path on the (f) Pd surface and (g) surface. The balls in cyan, gold, red, grey, and white represent Pd, Au, O, C, and H atoms, respectively. (For interpretation of the references to colour in this figure, the reader is referred to the web version of this article.)

$\text{CH}_3\text{OOH}$ ) formation stage (stage-II). The  $\text{CH}_3\text{OOH}$  produced in the  $\text{CH}_3\text{OOH}$  path would be further oxidized to  $\text{CH}_3\text{OH}$ . All the relevant structures are summarized (Figs. S15, S16). The energy barrier ( $E_b$ ), defined as the energy difference between the initial state and the highest transition state, in each elementary reaction are evaluated to access the  $\text{CH}_4$  oxidation performance of the catalyst. For the Pd slab, the  $E_b$  is estimated to be 1.21 eV ( $\text{I} \rightarrow \text{TS2}$ ) and 1.19 eV ( $\text{I} \rightarrow \text{TS3}$ ) for  $\text{CH}_3\text{OH}$  and  $\text{CH}_3\text{OOH}$  path, respectively (Fig. 5f). At stage-I,  $\text{CH}_3^*$  groups are produced by the reaction of  $\text{CH}_4$  and  $\text{OH}^*$  with an  $E_b$  of 0.90 eV ( $\text{I} \rightarrow \text{II}$ ). Afterwards, the reaction of stage-II for  $\text{CH}_3\text{OH}$  path ( $\text{III} \rightarrow \text{IV}$ ) exhibits a high  $E_b$  of 1.42 eV due to the strong adsorption of  $\text{CH}_3^*$  on the Pd surface. Note that in the stage-II for the  $\text{CH}_3\text{OOH}$  path, there are two transition states, the decomposition of  $\text{OOH}^*$  to produce  $\text{CH}_3\text{O}^*$  and  $\text{OH}^*$  ( $\text{V} \rightarrow \text{VI}$ ,  $E_{b3} = 1.55$  eV) and the thermodynamically unfavorable  $\text{CH}_3\text{OOH}^*$  formation ( $\text{VI} \rightarrow \text{VII}$ ,  $E_{b4} = 1.32$  eV), which suggests that the  $\text{CH}_3\text{OOH}$  path is limited on the Pd surface. As illustrated in Fig. 5g, the elementary reactions are all exothermic on the PdAu surface, and the  $E_b$  of stage-II for  $\text{CH}_3\text{OH}$  and  $\text{CH}_3\text{OOH}$  path is 1.17 ( $\text{III} \rightarrow \text{TS2}$ ) and 1.03 eV ( $\text{V} \rightarrow \text{TS3}$ ), respectively, much smaller than those (1.32 ~ 1.55 eV) on the pure Pd surface owing to the weaker adsorption of  $\text{CH}_3^*$  on PdAu surface, implying that both of  $\text{CH}_3\text{OH}$  and  $\text{CH}_3\text{OOH}$  formation on PdAu surface are accelerated. Moreover, the apparent  $E_b$  is 1.03 eV ( $\text{I} \rightarrow \text{TS1}$ ) on the AuPd surface, also smaller than those on the pure Pd surface (1.19 ~ 1.21 eV). The DFT results demonstrate that alloying with Au enables to modulate the adsorption strength between the intermediate radicals and Pd atom, and the reaction pathways can also be optimized, promoting the direct conversion of  $\text{CH}_4$  to C1 products.

#### 4. Conclusions

In summary,  $\text{Pd}_x\text{Au}_y$  NWs with high quality are systematically investigated for the structure-activity relationship between PdAu and the  $\text{CH}_4$  oxidation performance. The experimental results indicate that the unique 1D structure, the compositions of PdAu NWs and the reaction conditions affect the performance of the direct  $\text{CH}_4$  oxidation to liquid C1 products.  $\text{Pd}_9\text{Au}_1$  NWs show a maximum yield of  $2890.3 \mu\text{mol g}^{-1} \text{h}^{-1}$  and a 99% selectivity for liquid C1 products at  $70^\circ\text{C}$ . More importantly, the probably reaction pathways for the direct  $\text{CH}_4$  oxidation to C1 products are proposed, and DFT results clearly reveal that the moderated binding strength between the intermediates ( $\text{OH}^*$ ,  $\text{OOH}^*$ ,  $\text{CH}_3^*$ ) and Pd atoms by the incorporation of Au facilitates the C-H activation and targeted products generation. This study provides deep insights to improve the performance of PdAu catalysts in the direct  $\text{CH}_4$  conversion to high added-value chemical feedstocks.

#### CRediT authorship contribution statement

**Yueshan Xu:** Conceptualization, Investigation, Visualization, Writing – original draft. **Daoxiong Wu:** Investigation, Resources, Visualization, Writing – original draft. **Peilin Deng:** Conceptualization, Investigation, Writing – original draft, Resources. **Jing Li:** Investigation, Resources. **Junming Luo:** Investigation, Resources. **Qi Chen:** Investigation. **Wei Huang:** Investigation. **Chong Michael Shim:** Investigation. **Chunman Jia:** Investigation. **Zhongxin Liu:** Investigation. **Yijun Shen:** Investigation. **Xinlong Tian:** Conceptualization, Project administration, Supervision, Resources, Writing – review & editing.

#### Declaration of Competing Interest

The authors declare that they have no known competing financial interests or personal relationships that could have appeared to influence the work reported in this paper.

#### Acknowledgments

This work was supported by the Hainan Province Science and

Technology Special Fund (ZDYF2020037, 2020207), the National Natural Science Foundation of China (21805104, 22109034, 22109035, 52164028, 62105083), the Postdoctoral Science Foundation of Hainan Province (RZ2100007123), the Innovative Research Projects for Graduate Students of Hainan Province (Qhyb2021-20), the Basic and Applied Basic Research Foundation of Guangdong Province (2019A1515110558), the Research Fund Program of Key Laboratory of Fuel Cell Technology of Guangdong Province (2020201) and the Start-up Research Foundation of Hainan University (KYQD(ZR)-20008, 20082, 20083, 20084, 21065, 21125).

#### Appendix A. Supporting information

Supplementary data associated with this article can be found in the online version at doi:10.1016/j.apcatb.2022.121223.

#### References

- [1] X. Meng, X. Cui, N.P. Rajan, L. Yu, D. Deng, X. Bao, Chem 5 (2019) 2296–2325.
- [2] X. Tang, L. Wang, B. Yang, C. Fei, T. Yao, W. Liu, Y. Lou, Q. Dai, Y. Cai, X.-M. Cao, W. Zhan, Y. Guo, X.-Q. Gong, Y. Guo, Appl. Catal., B 285 (2021), 119827.
- [3] M.S.A. Sher Shah, C. Oh, H. Park, Y.J. Hwang, M. Ma, J.H. Park, Adv. Sci. 7 (2020) 2001946.
- [4] P. Schwach, X. Pan, X. Bao, Chem. Rev. 117 (2017) 8497–8520.
- [5] P. Tang, Q. Zhu, Z. Wu, D. Ma, Energy Environ. Sci. 7 (2014) 2580–2591.
- [6] M. Li, J. Shan, G. Giannakakis, M. Ouyang, S. Cao, S. Lee, L.F. Allard, M. Flytzani-Stephanopoulos, Appl. Catal., B 292 (2021), 120124.
- [7] K. Zhu, S. Liang, X. Cui, R. Huang, N. Wan, L. Hua, H. Li, H. Chen, Z. Zhao, G. Hou, Nano Energy 82 (2021), 105718.
- [8] M. Zhong, Y. Xu, J. Li, Z.-X. Ge, C. Jia, Y. Chen, P. Deng, X. Tian, J. Phys. Chem. C. 125 (2021) 12713–12720.
- [9] T. Moteki, N. Tominaga, M. Ogura, Appl. Catal., B 300 (2022), 120742.
- [10] K.T. Dinh, M.M. Sullivan, K. Narsimhan, P. Serna, R.J. Meyer, M. Dinca, Y. Roman-Leshkov, J. Am. Chem. Soc. 141 (2019) 11641.
- [11] M.A. Newton, A.J. Knorpp, V.L. Sushkevich, D. Palagin, J.A. van Bokhoven, Chem. Soc. Rev. 49 (2020) 1449–1486.
- [12] M. Ravi, V.L. Sushkevich, A.J. Knorpp, M.A. Newton, D. Palagin, A.B. Pinar, M. Ranocchiai, J.A. van Bokhoven, Nat. Catal. 2 (2019) 485–494.
- [13] B. Li, X. Song, S. Feng, Q. Yuan, M. Jiang, L. Yan, Y. Ding, Appl. Catal. B 293 (2021), 120208.
- [14] Z. Yi, Z. Tang, X. Wu, A. Huang, X. Luo, G.Q. Xu, Y. Zhu, S.L. Wang, Appl. Catal. B 306 (2021), 120919.
- [15] A.A. Latimer, A.R. Kulkarni, H. Aljama, J.H. Montoya, J.S. Yoo, C. Tsai, F. Abild-Pedersen, F. Studt, J.K. Nørskov, Nat. Mater. 16 (2017) 225–229.
- [16] M.A. Newton, A.J. Knorpp, A.B. Pinar, V.L. Sushkevich, D. Palagin, J.A. van Bokhoven, J. Am. Chem. Soc. 140 (2018) 10090–10093.
- [17] M.H. AbRahim, M.M. Forde, R.L. Jenkins, C. Hammond, Q. He, N. Dimitratos, J. A. Lopez-Sanchez, A.F. Carley, S.H. Taylor, D.J. Willock, D.M. Murphy, C.J. Kiely, G.J. Hutchings, Angew. Chem. Int. Ed. 52 (2013) 1280–1284.
- [18] M. Zhong, Y. Xu, J. Li, Z.-X. Ge, C. Jia, Y. Chen, P. Deng, X. Tian, J. Phys. Chem. C 125 (2021) 12713–12720.
- [19] M.H. Ab Rahim, R.D. Armstrong, C. Hammond, N. Dimitratos, S.J. Freakley, M. M. Forde, D.J. Morgan, G. Lalev, R.L. Jenkins, J.A. Lopez-Sanchez, S.H. Taylor, G. J. Hutchings, Catal. Sci. Technol. 6 (2016) 3410–3418.
- [20] R. McMicker, N. Agarwal, S.J. Freakley, Q. He, S. Althahban, S.H. Taylor, C.J. Kiely, G.J. Hutchings, Catal. Today 342 (2020) 32–38.
- [21] N. Agarwal, S.J. Freakley, R.U. McMicker, S.M. Althahban, N. Dimitratos, Q. He, D. J. Morgan, R.L. Jenkins, D.J. Willock, S.H. Taylor, C.J. Kiely, G.J. Hutchings, Science 358 (2017) 223–227.
- [22] Z. Jin, L. Wang, E. Zuidema, K. Mondal, M. Zhang, J. Zhang, C. Wang, X. Meng, H. Yang, C. Mesters, F.-S. Xiao, Science 367 (2020) 193–197.
- [23] R. Serra-Maia, F.M. Michel, Y. Kang, E.A. Stach, ACS Catal. 10 (2020) 5115–5123.
- [24] Y. He, J. Liang, Y. Imai, K. Ueda, H. Li, X. guo, G. Yang, Y. Yoneyama, N. Tsubaki, Catal. Today 352 (2020) 104–110.
- [25] W. Huang, S. Zhang, Y. Tang, Y. Li, L. Nguyen, Y. Li, J. Shan, D. Xiao, R. Gagne, A. I. Frenkel, F. Tao, Angew. Chem. Int. Ed. 55 (2016) 13441–13445.
- [26] X. Tian, X. Zhao, Y.-Q. Su, L. Wang, H. Wang, D. Dang, B. Chi, H. Liu, J.M. Hensen Emiel, W. Lou Xiong, Y. Xia Bao, Science 366 (2019) 850–856.
- [27] M. Li, Z. Zhao, T. Cheng, A. Fortunelli, C.-Y. Chen, R. Yu, Q. Zhang, L. Gu, V. Merinov Boris, Z. Lin, E. Zhu, T. Yu, Q. Jia, J. Guo, L. Zhang, A. Goddard William, Y. Huang, X. Duan, Science 354 (2016) 1414–1419.
- [28] G. Kresse, J. Furthmüller, Phys. Rev. B: Condens. Matter 54 (1996) 11169–11186.
- [29] G. Kresse, J. Furthmüller, Comput. Mater. Sci. 6 (1996) 15–50.
- [30] J.P. Perdew, K. Burke, M. Ernzerhof, Phys. Rev. Lett. 77 (1996) 3865–3868.
- [31] P.E. Blöchl, Phys. Rev. B 50 (1994) 17953–17979.
- [32] G. Kresse, D. Joubert, Phys. Rev. B 59 (1999) 1758–1775.
- [33] S. Grimme, J. Antony, S. Ehrlich, H. Krieg, J. Chem. Phys. 132 (2010), 154104.
- [34] S. Grimme, S. Ehrlich, L. Goerigk, J. Comp. Chem. 32 (2011) 1456–1465.
- [35] R. Dronskowski, P.E. Blöchl, J. Phys. Chem. 97 (1993) 8617–8624.
- [36] V.L. Deringer, A.L. Tchougréeff, R. Dronskowski, J. Phys. Chem. A 115 (2011) 5461–5466.

- [37] S. Maintz, V.L. Deringer, A.L. Tchougréeff, R. Dronskowski, *J. Comp. Chem.* 34 (2013) 2557–2567.
- [38] S. Maintz, V.L. Deringer, A.L. Tchougréeff, R. Dronskowski, *J. Comput. Chem.* 37 (2016) 1030–1035.
- [39] G. Henkelman, B.P. Uberuaga, H. Jónsson, *J. Chem. Phys.* 113 (2000) 9901–9904.
- [40] K. Mathew, R. Sundaraman, K. Letchworth-Weaver, T.A. Arias, R.G. Hennig, *J. Chem. Phys.* 140 (2014), 084106.
- [41] K. Mathew, V.S.C. Kolluru, S. Mula, S.N. Steinmann, R.G. Hennig, *J. Chem. Phys.* 151 (2019), 234101.
- [42] V. Wang, N. Xu, J.-C. Liu, G. Tang, W.-T. Geng, *Comput. Phys. Commun.* 267 (2021), 108033.
- [43] K. Momma, F. Izumi, *J. Appl. Crystallogr.* 44 (2011) 1272–1276.
- [44] X. Huang, N. Zheng, *J. Am. Chem. Soc.* 131 (2009) 4602–4603.
- [45] J. Wang, P. Zhang, Y. Xiahou, D. Wang, H. Xia, H. Möhwald, *ACS Appl. Mater. Interfaces* 10 (2018) 602–613.
- [46] T. Ricciardulli, S. Gorthy, J.S. Adams, C. Thompson, A.M. Karim, M. Neurock, D. W. Flaherty, *J. Am. Chem. Soc.* 143 (2021) 5445–5464.
- [47] V. Fung, Z. Wu, D.-e Jiang, *J. Phys. Chem. Lett.* 9 (2018) 6321–6325.
- [48] Z. Wang, Z. Zheng, Y. Xue, F. He, Y. Li, *Adv. Energy Mater.* 11 (2021) 2101138.
- [49] H. Niu, X. Wang, C. Shao, Z. Zhang, Y. Guo, *ACS Sustain. Chem. Eng.* 8 (2020) 13749–13758.
- [50] C. Zhang, D. Wang, Y. Wan, R. Lv, S. Li, B. Li, X. Zou, S. Yang, *Mater. Today* 40 (2020) 18–25.